Title
Electronic structure of p-type transparent conducting oxide CuAlO2

Authors
Salah, Mohamed
Yoon, Joonseok
El-Desoky, Mohamed M
et al.

Publication Date
2022-07-01

DOI
10.1016/j.cap.2022.04.005

Peer reviewed

Electronic structure of *p*-type transparent conducting oxide $CuAlO_2$

Mohamed Salah[1,2], Joonseok Yoon[3], Mohamed M. El-Desoky[2], Zahid Hussain[1], Honglyoul Ju[3], and Sung-Kwan Mo[1,*]

[1]*Advanced Light Source, Lawrence Berkeley National Laboratory, Berkeley, CA 94720, USA*
[2]*Department of Physics, Faculty of Science, Suez University, Suez 43518, Egypt*
[3]*Department of Physics, Yonsei University, Seoul 120-749, Korea*

**e-mail: SKMo@lbl.gov*

Abstract

Copper-based delafossite oxides are excellent candidates for the *p*-type transparent conducting oxide (TCO), which is essential in realizing transparent semiconductor applications. Using angle-resolved photoemission spectroscopy (ARPES), we report the low-energy electronic structure of $CuAlO_2$. We found that the band structure near the valence band top is characterized by hole bands with their maxima along the Brillouin zone boundary. Furthermore, the effective masses along the Γ–M and Γ–K directions were found to be $(0.6 \pm 0.1)\ m_0$ and $(0.9 \pm 0.1)\ m_0$, respectively, which impose an important benchmark against the existing band calculations.

The combination of light transmission in the visible spectrum and electrical conductivity forms the basis of transparent conducting oxides (TCOs). TCOs are generally scarce but important for numerous technological applications, including flat panel displays, solar cells, smart windows, gas sensors, and transparent transistors [1-12]. Most known high-performance TCOs tend to be *n*-type materials, for example, indium tin oxide (ITO) [13, 14] , fluorine tin oxide (FTO) [15, 16], and zinc oxide (ZnO) [17-19]. Kawazoe *et al.* discovered an efficient *p*-type TCO in the delafossite $CuAlO_2$ with room temperature conductivity (σ) as high as 1 S cm^{-1} and mobility (μ) about 10 $cm^2V^{-1}s^{-1}$. Moreover, the positive Seebeck coefficient of $CuAlO_2$ points to that the majority of carriers are holes [11]. On the other hand, it was found that there currently exists a gap in our understanding between *p*-type and *n*-type TCOs, which hinders the improvement of *p*-*n* junction TCO-based devices [20, 21]. As a result, a plenty of delafossites were discovered to enhance the conductivity of *p*-type TCO materials, for instance $CuBO_2$ [22], $CuCrO_2$ [23], $CuGaO_2$ [24], $CuInO_2$ [25] and $CuYO_2$ [26], as well as $SrCu_2O_2$ [12].

Cu-based delafossites have been studied intensively in order to predict the bandgap, understand the conductivity, investigate the physical properties of the materials and improve their efficiency. As a result, several band structure calculations have been performed using the density functional theory (DFT) under the local density approximation (LDA) and using various approximations and hybrid functionals [27-47]. However, the key parameters resulting from the theoretical efforts are largely scattered. For example, the effective mass and bandgap size of $CuAlO_2$ range from 0.42 m_0 to 8 m_0 and 1.9 eV to 13 eV, respectively. Although, it is generally believed that the effective mass of less than 1.5 m_0 and the bandgap smaller than 3 eV are advantageous in realizing a TCO to accomplish a simultaneous high conductivity and excellent transparency to visible light [5].

There have been only a small number of experimental studies reported until now. The experimental bandgap has been reported to be between 2.2 eV and 4.2 eV [48-53] from optical spectroscopy and the combination of x-ray emission (XES) and x-ray absorption spectroscopy (XAS). In this work, we report a study using the angle-resolved photoemission spectroscopy (ARPES) on $CuAlO_2$ to reveal a detailed picture of the momentum resolved electronic structure. We have found that the top of the valence band is dominated by the hole bands around the

hexagonal Brillouin zone boundary. The electron removal gap is found to be ~ 0.3 eV with the valence band top near the K point. The experimental effective masses along the Γ–M and Γ–K directions are determined from the band structure to be (0.6 ± 0.1) m_0 and (0.9 ± 0.1) m_0, respectively.

The single-crystal of $CuAlO_2$ was synthesized using the flux self-removal method as described in Ref. [53]. The ARPES experiments were carried out at the Beamline 10.0.1 of the Advanced Light Source at Lawrence Berkeley National Laboratory, using a Scienta R4000 electron analyzer. The base pressure of the experimental endstation was 3×10^{-11} Torr. The photon energy was set to 55 eV with a total convolved energy and an angular resolution of 25 meV and 0.9°, respectively. The measurement temperature was 300 K. Below 200K, we found signatures of sample charging.

Figure 1 shows the crystal structure and the Brillouin zone of $CuAlO_2$. It has a layered crystal structure illustrated in Fig. 1(a), characterized by the space group of $\bar{R}3m$ in the normal phase. It consists of O-Cu-O dumbbell layers in a hexagonal plane separated by an AlO_6 edge-sharing octahedra layer with lattice parameters $a = b = 2.858$ Å and $c = 16.96$ Å [38, 54]. Fig. 1(b) displays the bulk and surface-projected Brillion zone of delafossite 3R-phase $CuAlO_2$ with high symmetry points labeled.

The overall electronic structure of $CuAlO_2$ measured by ARPES is summarized in Figure 2. Fig. 2(a) shows the angle-integrated photoemission spectrum of $CuAlO_2$, which represent the total density of states clearly illustrating the characteristics of the Cu 3*d* and O 2*p* originated valence state. The overall intensity is dominated by the O 2*p* state in higher binding energy (-6 eV to ~ -1.5 eV). The Cu 3*d* state close to the Fermi energy is weaker in intensity but is well separated from the O 2*p* state and clearly visible. Previous x-ray measurements [50] found that non-negligible mixing of orbital characters between O 2*p* and Cu 3*d* states exists. The O 2*p* states in higher binding energy clearly show dispersive features along the high symmetry direction, as depicted in Fig. 2(b), which shows single crystallinity and high surface quality of the sample. The dispersion of the valence states close to chemical potential is only visible when zoomed in (Fig. 2(c)) due to the significant difference in intensity between O 2*p* and Cu 3*d* states. We found

a hole band disperses towards the Brillouin zone boundary along the Γ–K direction with finite intensity up to 300 meV below the Fermi energy. The visibility of this dispersive band is dependent on the experimental geometry. The spectrum shown in Fig. 2(c) is measured with linear polarization of the light is in the plane of the sample surface and detection plane perpendicular to the light polarization. A clearer view of this feature can be made within a different geometry and presented below.

Figure 3 shows the iso-energy surfaces of $CuAlO_2$ at different binding energies. At Fermi level (Fig. 3(a)), there is hardly any state shown in the intensity map, confirming the insulating nature of the sample. Moving to the higher binding energy, E = -0.4 eV (Fig. 3(b)), the iso-energy surface map show the intensity from the valence band top. We found the signal from the valence band top is mainly concentrated along the Brillouin zone boundary. Moving further down in energy to -0.9 eV and -1.4 eV (Figs. 3(c) and (d)), the intensity formerly concentrated along the zone boundary splits to form hexagonal constant energy contours encapsulating the Γ point. The evolution of iso-energy surface with the increasing binding energy confirms the hole nature of the low energy valence band and carriers excited from it.

We now focus on the dispersion along the high-symmetry lines of the low energy valence hole bands. Figure 4 shows the dispersion of the hole bands along the Γ–K and Γ–M directions in intensity maps and energy distribution curve (EDC) stacks. The data shown here are measured in the geometry where the electron detection plane is parallel to the light polarization to better visualize the low intensity near Fermi energy features. The valence band maximum (VBM) position is slightly different at the K point and at the M point, -0.3 eV and -0.5 eV, respectively, which correspond to the size of the electron removal gaps. The size of the full gap cannot be estimated from the photoemission data alone since the unoccupied state above the Fermi energy cannot be measured by electron removal spectroscopy such as ARPES. However, according to electronic structure calculation employing GGA+PBE [31], the conduction band minimum (CBM) can be identified at the Γ point at an energy of around 2 eV relative to the Fermi level, which corresponds to an indirect gap of about 2.3 eV. This is consistent with previous XES and XAS measurements [50]. Our preliminary XES and XAS measurements (not shown) also confirms the gap of a similar size. The optical measurements on the same crystal used here [53]

also report an indirect gap of similar size ~ 2.2eV although it tends to underestimate the size of the gap [55, 56]. The exact size of the full gap of $CuAlO_2$ requires further studies by optical measurements, scanning tunneling spectroscopy or high-resolution XES and XAS measurements.

The hole effective mass (m^*) can be estimated from our experimental dispersion relations. Using the relation $1/m^* = 1/h^2\ (dE^2/d^2k)$ and simple parabolic approximation, we estimate m^* along the Γ–M direction $m^*_{\Gamma M} = (0.6 \pm 0.1)\ m_0$. In the same way, the effective mass along the Γ–K direction is found to be $m^*_{\Gamma K} = (0.9 \pm 0.1)\ m_0$. These values reasonably agree with the GGA+PBE predicted effective masses of 0.58 m_0 for the Γ–M direction [31] . The relation between electrical conductivity (σ) and carrier mobility (μ) of TCO materials is directly proportional ($\sigma = ne\mu$), where (e) is the elementary charge, and (n) is the charge carrier concentration, while the relationship between charge carrier mobility (μ) and the effective mass (m^*) is inversely proportional ($\mu = e\tau/m^*$), where (τ) is the free carrier scattering time. The effective mass is a crucial quantity to determine the transport properties. In *p*-type semiconductors, a faster dispersion at the VBM indicates a low hole effective mass, which corresponds to high carrier mobility and hence high electrical conductivity [5]. The small hole effective mass of $CuAlO_2$ obtained from ARPES is consistent with the high mobility and conductivity of the transport measurements [11].

In summary, we have used ARPES to clarify the electronic structure of the delafossite $CuAlO_2$. Our data are consistent with the previous report that $CuAlO_2$ is an indirect bandgap *p*-type TCO. Our ARPES results are in good agreement with a recent theoretical report [31] on the overall electronic structure, effective mass, and bandgap size. The hole effective mass of $CuAlO_2$ has been identified as small as $m^*_{\Gamma M} = (0.6 \pm 0.1)\ m_0$. Given the size of the experimental optical bandgap of around ~ 2.5 eV, this implies good conductivity and a wide bandgap. Our results provide an essential benchmark for the available theoretical calculations and future studies on the electronic properties of TCO $CuAlO_2$.

Acknowledgments

The work performed at the Advanced Light Source was supported by the Office of Basic Energy Sciences, the US Department of Energy, under Contract No. DE-AC0205CH11231. M.S. was funded by a scholarship (JS3809) from the Ministry of Higher Education of Egypt.

References

[1] R. Liu, Y. Li, B. Yao, Z. Ding, R. Deng, L. Zhang, H. Zhao, L. Liu, Journal of Physics D: Applied Physics, 48 (2015) 335102.

[2] P.P. Edwards, A. Porch, M.O. Jones, D.V. Morgan, R.M. Perks, Dalton Transactions, (2004) 2995.

[3] C.G. Granqvist, Solar Energy Materials and Solar Cells, 91 (2007) 1529.

[4] G.A. Niklasson, C.G. Granqvist, Journal of Materials Chemistry, 17 (2007) 127.

[5] K.H.L. Zhang, K. Xi, M.G. Blamire, R.G. Egdell, Journal of Physics: Condensed Matter, 28 (2016) 383002.

[6] A. Buljan, M. Llunell, E. Ruiz, P. Alemany, Chemistry of Materials, 13 (2001) 338-344.

[7] H. Ohta, H. Hosono, Materials Today, 7 (2004) 42.

[8] Z.W. Pan, Z.R. Dai, Z.L. Wang, Science, 291 (2001) 1947.

[9] E. Comini, G. Faglia, G. Sberveglieri, Z. Pan, Z.L. Wang, B. N., S.-B. M., G. W., Applied Physics Letters, 81 (2002) 1869.

[10] M. Batzill, U. Diebold, Progress in Surface Science, 79 (2005) 47.

[11] H. Kawazoe, M. Yasukawa, H. Hyodo, M. Kurita, H. Yanagi, H. Hosono, Nature, 389 (1997) 939.

[12] A. Kudo, H. Yanagi, H. Hosono, H. Kawazoe, Appl. Phys. Lett., 73 (1998) 220.

[13] S.H. Jeong, S.B. Lee, J.H. Boo, Current Applied Physics, 4 (2004) 655.

[14] J. Gao, O.I. Lebedev, S. Turner, Y.F. Li, Y.H. Lu, Y.P. Feng, P. Boullay, W. Prellier, G. van Tendeloo, T. Wu, Nano Letters, 12 (2012) 275.

[15] Y. Li, R. Deng, Y. Tian, B. Yao, T. Wu, Ž. I., F. J., D.S. S., Applied Physics Letters, 100 (2012) 172402.

[16] Y. Li, W. Yin, R. Deng, R. Chen, J. Chen, Q. Yan, B. Yao, H. Sun, S.-H. Wei, T. Wu, NPG Asia Materials, 4 (2012) e30.

[17] S.-M. Jung, Y.-H. Kim, S.-I. Kim, S.-I. Yoo, Current Applied Physics: Supplement, 11 (2011) S191.

[18] Y. Li, R. Deng, W. Lin, Y. Tian, H. Peng, J. Yi, B. Yao, T. Wu, Physical Review B, 87 (2013) 155151.
[19] M. Ali, M. Salah, M. El-Desoky, Frontiers in Scientific Research and Technology, 3 (2022) 78.
[20] K. Nomura, H. Ohta, K. Ueda, T. Kamiya, M. Hirano, H. Hosono, Science, 300 (2003) 1269.
[21] J. Cai, H. Gong, G. H., W. Y., L. Y., Journal of Applied Physics, 98 (2005) 033707.
[22] C. Ruttanapun, S. A., Journal of Applied Physics, 114 (2013) 113108.
[23] R. Nagarajan, A.D. Draeseke, A.W. Sleight, J. Tate, R.D. B., S.R. D., P.C. T., G.J. L., Journal of Applied Physics, 89 (2001) 8022.
[24] K. Ueda, T. Hase, H. Yanagi, H. Kawazoe, H. Hosono, H. Ohta, M. Orita, M. Hirano, K. H., Y. M., H. H., K. M., Y. H., H. H., Journal of Applied Physics, 89 (2001) 1790.
[25] M. Singh, V.N. Singh, B.R. Mehta, J Nanosci Nanotechnol, 8 (2008) 3889.
[26] D.J. Singh, Physical Review B, 77 (2008) 205126.
[27] A. Buljan, P. Alemany, E. Ruiz, The Journal of Physical Chemistry B, 103 (1999) 8060.
[28] X. Nie, S.-H. Wei, S.B. Zhang, Physical Review Letters, 88 (2002) 066405.
[29] H. Katayama-Yoshida, T. Koyanagi, H. Funashima, H. Harima, A. Yanase, Sol. Stat. Comm., 126 (2003) 135.
[30] I. Hamada, H. Katayama-Yoshida, Physica B, 376−377 (2006) 808.
[31] B. Falabretti, J. Robertson, H. I., G.C. G., Journal of Applied Physics, 102 (2007) 123703.
[32] M.N. Huda, Y. Yan, A. Walsh, S.-H. Wei, M.M. Al-Jassim, K. O., T.J. A., Applied Physics Letters, 94 (2009) 251907.
[33] D.O. Scanlon, G.W. Watson, Chem. Mater., 21 (2009) 5435.
[34] R. Laskowski, N.E. Christensen, P. Blaha, B. Palanivel, Physical Review B, 79 (2009) 165209.
[35] D.O. Scanlon, A. Walsh, G.W. Watson, Chemistry of Materials, 21 (2009) 4568.
[36] N.E. Christensen, A. Svane, R. Laskowski, B. Palanivel, P. Modak, A.N. Chantis, M.v. Schilfgaarde, T. Kotani, Physical Review B, 81 (2010) 045203.
[37] D.O. Scanlon, K.G. Godinho, B.J. Morgan, G.W. Watson, J. Chem. Phys., 132 (2010) 024707.
[38] D.O. Scanlon, G.W. Watson, The Journal of Physical Chemistry Letters, 1 (2010) 3195.

[39] F. Trani, J. Vidal, S. Botti, M.A.L. Marques, Physical Review B, 82 (2010) 085115.
[40] J. Vidal, F. Trani, F. Bruneval, M.A.L. Marques, S. Botti, Phys. Rev. Lett., 104 (2010) 136401.
[41] M.N. Huda, Y. Yan, M.M. Al-Jassim, K. O., T.J. A., Journal of Applied Physics, 109 (2011) 113710.
[42] K.G. Godinho, B.J. Morgan, J.P. Allen, D.O. Scanlon, G.W. Watson, J Phys Condens Matter, 23 (2011) 334201.
[43] A. Nakanishi, H. Katayama-Yoshida, Journal of the Physical Society of Japan, 80 (2011) 053706.
[44] H. Dixit, R. Saniz, S. Cottenier, D. Lamoen, B. Partoens, Journal of Physics: Condensed Matter, 24 (2012) 205503.
[45] J. Robertson, R. Gillen, S.J. Clark, Thin Solid Films, 520 (2012) 3714.
[46] P. Poopanya, Physics Letters A, 379 (2015) 853.
[47] A. Nakanishi, H. Katayama-Yoshida, T. Ishikawa, K. Shimizu, Journal of the Physical Society of Japan, 85 (2016) 094711.
[48] H. Yanagi, S.-i. Inoue, K. Ueda, H. Kawazoe, H. Hosono, N. Hamada, K. H., Y. M., H. H., K. M., Y. H., H. H., Journal of Applied Physics, 88 (2000) 4159.
[49] A.N. Banerjee, R. Maity, P.K. Ghosh, K.K. Chattopadhyay, Thin Solid Films, 474 (2005) 261.
[50] D.J. Aston, D.J. Payne, A.J.H. Green, R.G. Egdell, D.S.L. Law, J. Guo, P.A. Glans, T. Learmonth, K.E. Smith, Physical Review B, 72 (2005) 195115.
[51] J. Pellicer-Porres, A. Segura, A.S. Gilliland, A. Munoz, n. Rodriguez-Hernandez, D. Kim, M.S. Lee, T.Y. Kim, Appl. Phys. Lett., 88 (2006) 181904.
[52] D.S. Kim, S.J. Park, E.K. Jeong, H.K. Lee, S.Y. Choi, Thin Solid Films, 515 (2007) 5103.
[53] J.S. Yoon, Y.S. Nam, K.S. Baek, C.W. Park, H.L. Ju, S.K. Chang, Journal of Crystal Growth, 366 (2013) 31.
[54] J. Tate, H.L. Ju, J.C. Moon, A. Zakutayev, A.P. Richard, J. Russell, D.H. McIntyre, Phys. Rev. B, 80 (2009) 165206.
[55] A. Dolgonos, T.O. Mason, K.R. Poeppelmeier, Journal of Solid State Chemistry, 240 (2016) 43.
[56] P. Makuła, M. Pacia, W. Macyk, The Journal of Physical Chemistry Letters, 9 (2018) 6814.

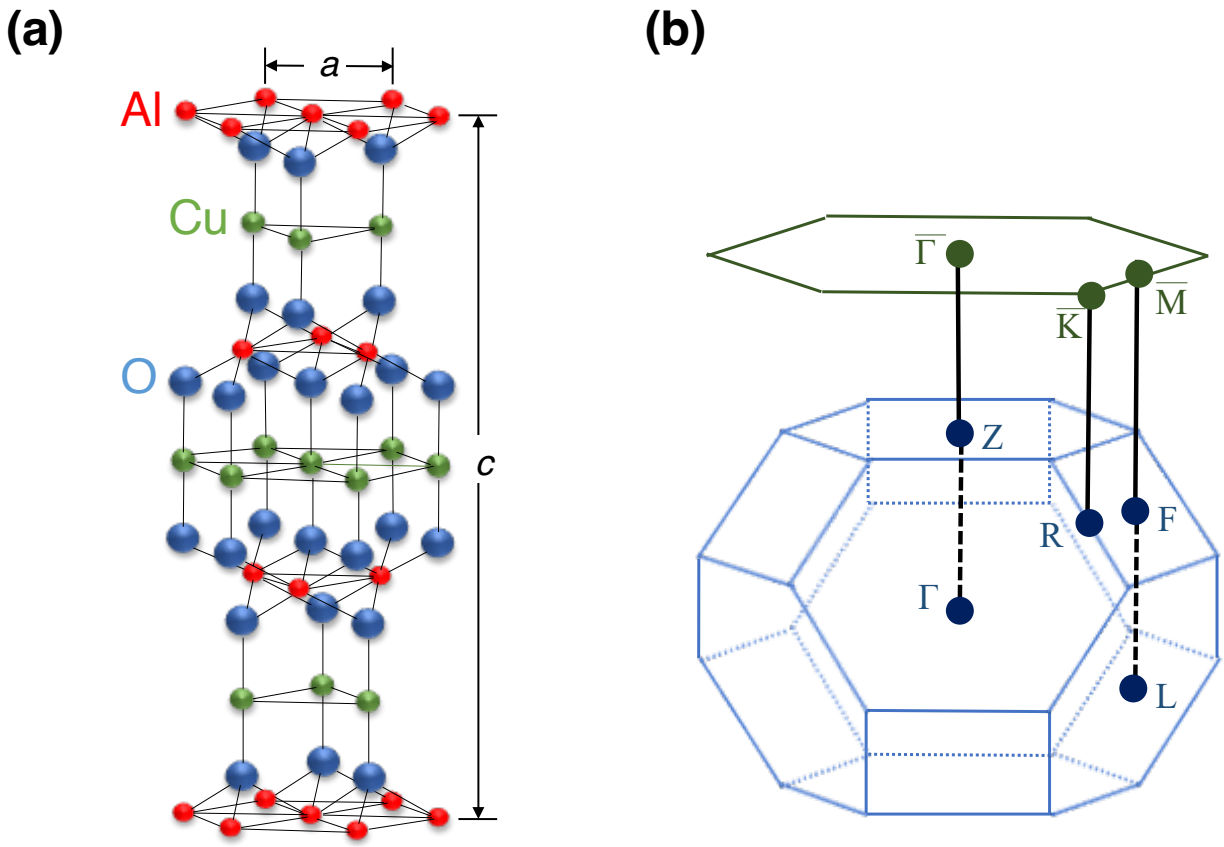

Figure 1. (a) Crystal structure of delafossite compound $CuAlO_2$, with copper, aluminum and oxygen atoms in green, red and blue, respectively. (b) Bulk (blue) and surface-projected (dark green) Brillouin zones with high symmetry points labeled.

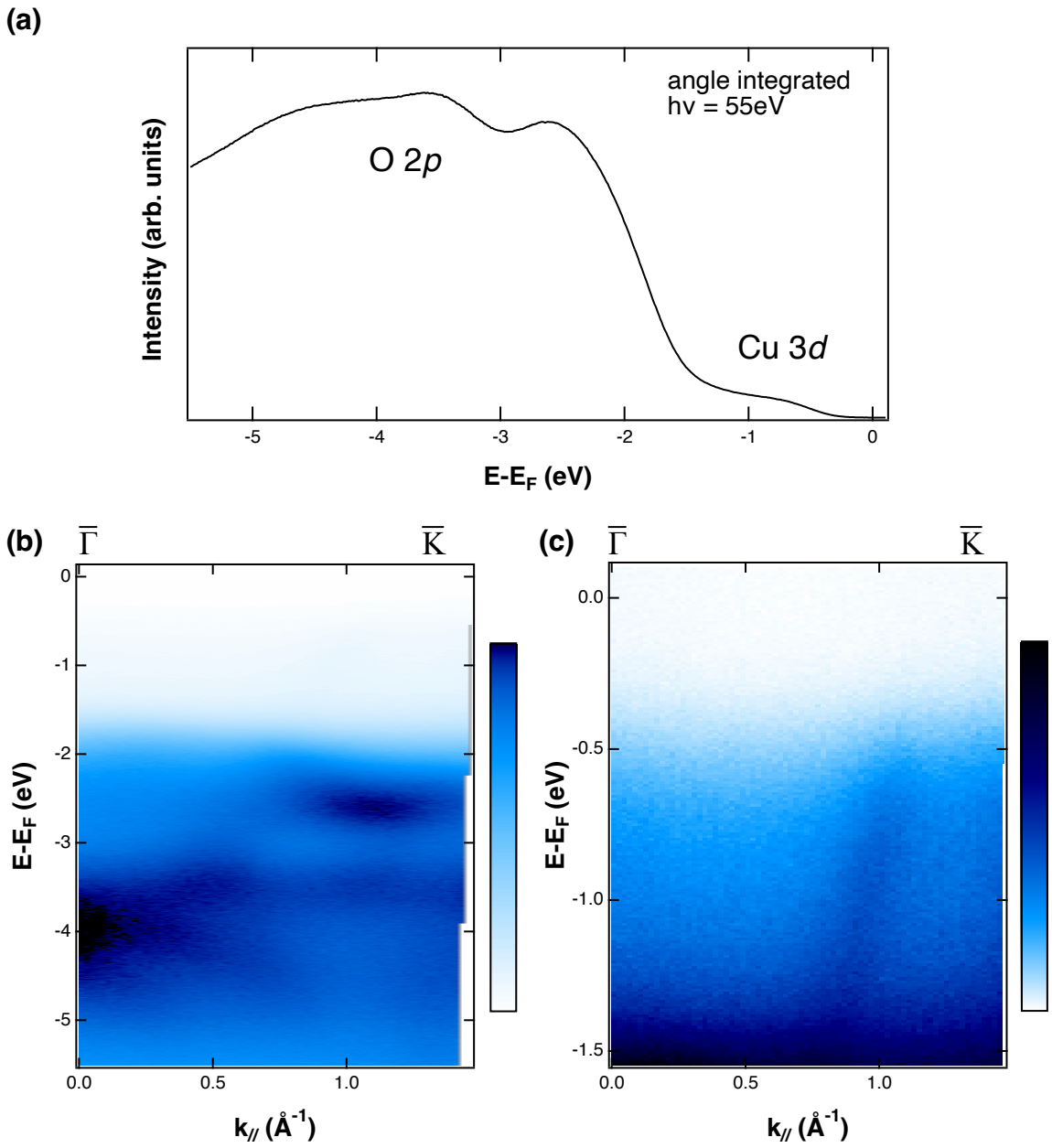

Figure 2. (a) Angle-integrated photoemission spectrum of $CuAlO_2$. (b) Angle-resolved photoemission intensity map along Γ–K direction. (c) Zoomed in the plot of dispersion map shown in (b) close to the Fermi energy.

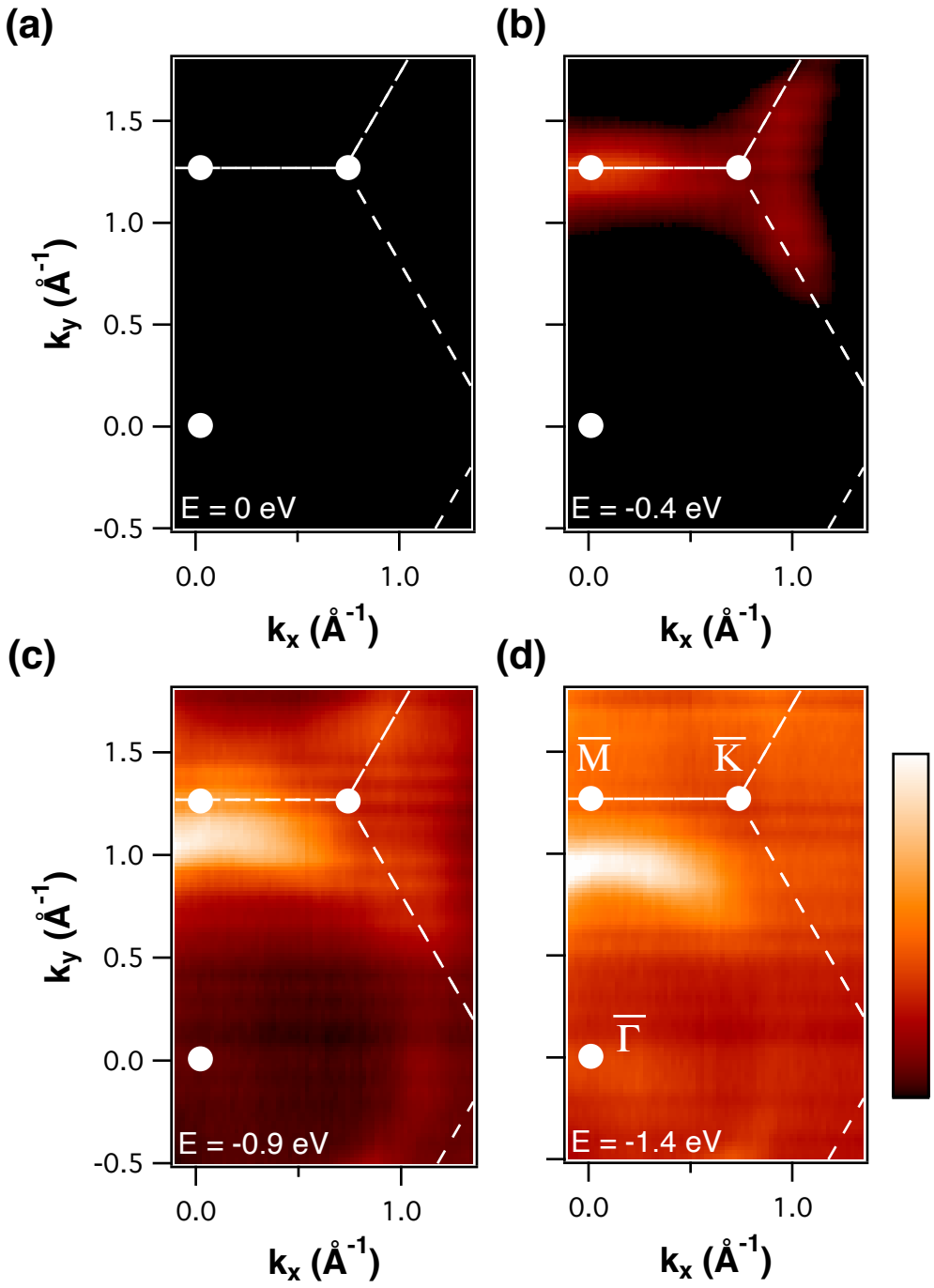

Figure 3. Iso-energy surface maps of $CuAlO_2$ at 0, -0.4, -0.9, and -1.4 eV relative to the Fermi energy, respectively. High symmetry points are marked in the plot.

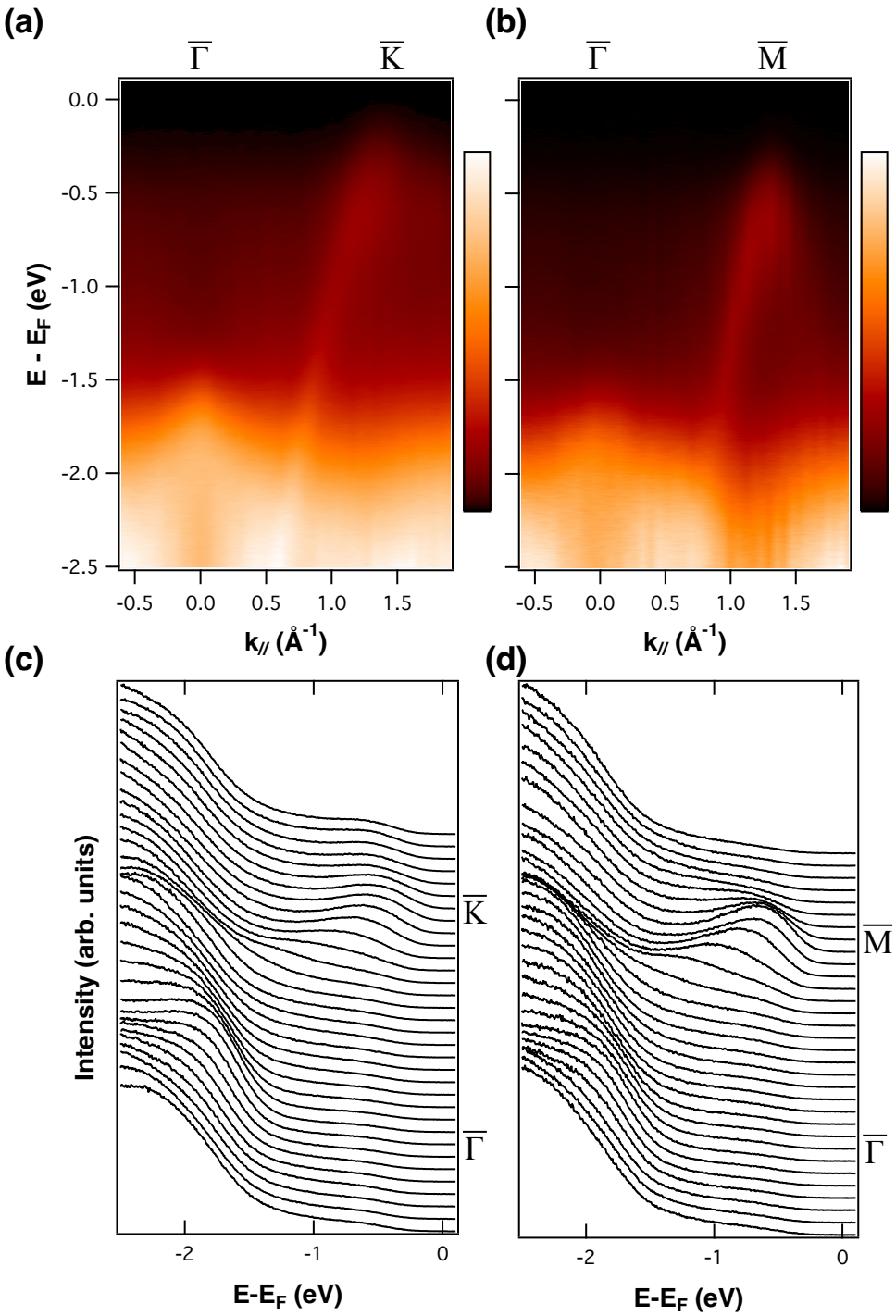

Figure 4. High-resolution ARPES spectra along Γ–K and Γ–M. (a), (c) ARPES intensity map and EDC stacks along the Γ–K direction. (b), (d) ARPES intensity map and EDC stacks along the Γ–M direction.